Analyst

PAPER

View Article Online
View Journal

Cite this: DOI: 10.1039/d6an00089d

Lipidomic signatures of CNS ischemic injury and their modulation by immunomodulatory hydrogels

Mary F. Wang, [a] Yunxin Ouyang, [b] Tatiana Segura *[b] and David C. Muddiman *[a]

Ischemic injury in the central nervous system (CNS) triggers profound metabolic remodeling that influences inflammation, repair, and cellular survival. Among these changes, lipids play key structural and signaling roles, yet the spatial distribution of lipid species after CNS ischemia, and how they respond to local immunomodulation, remains poorly understood. Here, we used infrared matrix-assisted laser desorption electrospray ionization mass spectrometry imaging (IR-MALDESI MSI) and immunofluorescence microscopy to map lipid and metabolite distributions in a mouse photothrombotic model of CNS ischemia. We first defined lipidomic shifts induced by ischemic injury alone, which included accumulation of sphingolipids and fatty acids (*e.g.*, ceramides, sphingomyelins, and polyunsaturated fatty acids) with concurrent depletion of glycerophospholipids (*e.g.*, phosphatidylethanolamines, phosphatidylcholines). We then examined how hyaluronic acid-based microporous annealed particle (MAP) hydrogels modulate these injury-associated lipid signatures. Injection of an immunomodulatory polysialic acid MAP (PSA-MAP) hydrogel altered cholesterol metabolism within the peri-infarct region of the lesion, increasing the ratio of cholesteryl ester to cholesterol—a lipid signature that inversely corresponds to cardiovascular disease states. Together, these data reveal that CNS ischemic injury drives characteristic lipid remodeling, and that biomaterial immunomodulation can reprogram this metabolic landscape toward a reparative state.

Received 25th January 2026,
Accepted 6th May 2026

DOI: 10.1039/d6an00089d

rsc.li/analyst

Introduction

Central nervous system (CNS) ischemia accounts for more than 80% of all strokes and are a leading cause of mortality worldwide and a primary cause of acquired physical disability in adults.[1,2] CNS ischemic injuries present a model of sterile inflammation which elicits profound metabolic reorganization.[3] Lipidomic remodeling is central to mitigating neuroinflammation post-injury as a response to cell death while initiating cell membrane repair and immune activation.[1,3] This metabolic reorganization varies across the stages of ischemic injury and wound healing wherein immune cells balance damage and neuroprotection in the acute stage and chronic CNS ischemic injuries further neurological damage through adaptive immune responses.[4]

Lipidomic remodeling in ischemic injuries (*e.g.*, stroke) is central to understanding the underlying pathology. Lipid species are one of the primary components of the brain accounting for 78% of dry weight in the axon myelin sheath and 35–40% of the gray matter.[5] Lipids play critical roles in cell membrane stability, inflammatory response, glial activation, and immune system resolution.[6,7] Dysregulation of glycerophospholipids and sphingolipids is strongly linked to impairment of the cell membrane in ischemic stroke.[1] Polyunsaturated fatty acids (PUFAs), a subtype of fatty acyls, contribute to resolution of inflammation and contribute immunomodulatory effects.[6,8] Glial cells, such as microglia, are regulated by various lipid species in the brain to prompt immune system responses to ischemic injury.[9]

While systemic lipid alterations following ischemic injury have been studied in depth, spatially resolved lipidomic remodeling in the brain and its subsequent alteration following biomaterial interventions remains poorly understood. This understanding of spatial lipidomic response to ischemic stroke and biomaterials may be investigated using mass spectrometry imaging (MSI) techniques. Similar studies have been conducted to study control models of CNS ischemic injury and other neurological disorders (*e.g.*, neurodegenerative disease) in rodent models using MALDI-MSI,[10–13] DESI-MSI,[14,15] and other MS imaging modalities. Infrared matrix-assisted laser desorption electrospray ionization (IR-MALDESI) MSI has been previously used to study wound healing in skin samples wherein, 594 lipid species were annotated across a 56-layer three-dimensional study in mouse skin[16] and the lipidomic response to wound healing was evaluated across three stages: inflammation, proliferation, and remodeling.[17] These prior

[a]*Biological Imaging Laboratory for Disease and Exposure Research (BILDER), Department of Chemistry, North Carolina State University, Raleigh, North Carolina, 27695, USA. E-mail: dcmuddim@ncsu.edu; Tel: +1 919-513-0084*
[b]*Department of Biomedical Engineering, Duke University, Durham, North Carolina, 27705, USA. E-mail: tatiana.segura@duke.edu; Tel: +1-919-660-2901*

studies provide context for the use of IR-MALDESI MSI to study wound healing as these methods demonstrate effective detection of a broad range of lipid species. Further, previous analyses have been conducted to optimize overall detection of small molecules (*e.g.*, lipids and metabolites) in mouse brain using sucrose-embedding with paraformaldehyde-fixation for IR-MALDESI MSI.[18,19] Other MS imaging modalities have been applied to the study of CNS ischemic stroke and other neurological disorders (*e.g.*, neurodegenerative disease) in rodent models using MALDI-MSI[10–13] and DESI-MSI.[14,15] Implementing IR-MALDESI MSI analyses provides a deeper understanding into how novel biomaterials interact and reprogram lipid species in the CNS.

Biomaterials such as microporous hyaluronic acid (HA) hydrogels have demonstrated their capacity to modulate local immune responses and wound healing.[20–24] Herein, they are used to probe how local immunomodulation influences CNS lipid metabolism. We hypothesized that CNS ischemic injury drives distinct lipidomic remodeling and that biomaterial immunomodulation alters these lipid signatures toward a reparative metabolic state.

Materials and methods

Materials

LC-MS-grade water (H_2O), acetonitrile (MeCN), absolute (200 proof) ethanol (EtOH), xylenes, and formic acid (FA) were purchased from Fisher Scientific (Nazareth, PA, United States). Tissues were sectioned and mounted on glass slides purchased from Globe Scientific (Mahwah, NJ, United States).

Photothrombotic stroke and stereotactic injection of hydrogel

Animal procedures were performed in accordance with the US National Institutes of Health Animal Protection Guidelines and approved by the Chancellor's Animal Research Committee as well as the Duke Office of Environment Health and Safety under protocol number A247-23-12. The PT stroke was induced using Rose Bengal photoactive dye as previously described (day 0).[25] All mice were between 8–12 weeks of age at the time of stroke.[25] The animals were anesthetized with isoflurane (3% induction and 1.5% maintenance at 1 L min^{-1} USP grade O_2) and placed on a stereotactic apparatus. After application of eye ointment and sterilization of the mouse's head, a midline incision was created to expose the skull, and connective tissue were removed. The laser was positioned 1.5 mm lateral from the bregma, and the mouse was interperitoneally (IP) injected with photosensitive dye Rose Bengal (Sigma; 10 mg mL^{-1} in PBS) at 10 μL g^{-1} mouse bodyweight. After 7 min, the brain was illuminated at 42 mW through intact skull for 13 min. A burr hole was drilled through the skull at 1.5 mm medial/lateral (same as laser position). The incision was then closed using Vetbond (3M, St Paul, MN). Mice were placed in a clean cage on a heat pad and monitored until awake and alert. A total of eight C57BL/6J mice underwent PT stroke without any hydrogel injection/treatment and accounted for the control stroke condition.

Nine total mice underwent PT stroke (day 0) and were injected with one of the two hydrogels (day 5): HA-MAP (n = 3) and PSA-MAP (n = 3). Mice were randomly assigned to experimental conditions within each cage to control for potential cage-specific confounding factors. For treatment injections, mice were first anesthetized with isoflurane at 3% and then transferred and positioned on a stereotactic stage for isoflurane maintenance at 1.5%. Following alcohol and iodine washes (3×), the skin covering the skull was re-opened, exposing the location of the photo-thrombotic stroke. A MAP treatment (4.5 μL) consisting of packed hydrogel microparticles and 0.25 mM tetrazine functionalized HA (HA-Tet) solution at a volume ratio of 5 : 1 was injected directly into the stroke cavity through a flat 30-gauge needle attached to a 25 μL Hamilton syringe (Hamilton, Reno, NV). A syringe pump was used to deliver treatments at an infusion rate of 1 μL min^{-1} at the same coordinates as the PT stroke laser irradiation (1.5 mm lateral from bregma and 0.75 mm ventral from the skull). Prior to injection, the syringe was lowered 0.75 mm into the infarct site. Five minutes after completion of the injection, the syringe was slowly lifted out of the infarct site. The incision was then closed using Vetbond (3M, St Paul, MN). The mice were placed in a clean cage on a heat pad and monitored until awake and alert.

Tissue removal and sucrose-embedding/PFA-fixation was completed prior to sectioning (day 15). The biological replicate/animal information is available in Table S1.

Hydrogel preparation

HA was modified with norbornene (HA-NB) and tetrazine (HA-Tet) as previously described.[26] HA-NB hydrogel microparticles (HMPs) were produced using a planar flow-focusing microfluidic device as described previously.[24] The gel precursor solution for the HMPs was made by dissolving HA-NB in 3 × 10^{-1} M HEPES pH 7.5, di-thiol MMP-sensitive linker peptide (Ac-GCRDGPQGIWGQDRCG-NH2, Genscript) (SH/HA ratio of 14), tris(2-carboxyethyl)phosphine (TCEP) (Sigma-Aldrich) (TCEP/SH ratio of 0.25), 5 × 10^{-4} M or 0 M (for the no RGD condition) RGD peptide (Ac-RGDSPGERCG-NH2, Genscript), and 9.90 × 10^{-3} M lithium phenyl(2,4,6-trimethylbenzoyl) phosphinate photoinitiator (LAP) (TCI America, Portland, OR, USA). The final HA-NB in the precursor solution should be at 3.4% (w/v). These types of HMPs were used for making HA-MAP. For PSA-MAP, the HMPs were modified with PSA *via* incubating HMPs with tetrazine-modified PSA (PSA-Tet) at 37 °C for 4 h with agitation every 1 h and washed with 1× PBS, as previously described.[27]

Tissue preparation

Following PT stroke preparation and hydrogel treatment as defined for each treatment/condition, tissues were sucrose-embedded and PFA-fixed as previously described.[19] Tissues were subsequently sectioned coronally using a Thermo Scientific CryostarNX50 cryostat to 20 μm thickness and thaw mounted on glass slides.

Immunofluorescence staining and imaging

Immunofluorescence (IF) staining and imaging are performed as previously described.[24] In preparation of IF staining, slides were warmed to room temperature. Slides were then washed in 1× TBS (Sigma, D8537) for 5 min three times. A blocking buffer, comprised of 1× TBS, 0.3% Triton-X, and 10% normal donkey serum (NDS), was used to block tissue samples at room temperature for 1–2 h. After preparation in blocking buffer, primary antibodies were left to incubate with tissue overnight at 4 °C. The next day, slides were washed in 1× TBS + 0.3% Triton-X for 10 min three times. Secondary antibodies and DAPI (1 : 1000), prepared in blocking buffer, were then left to incubate with tissue for 2 h at room temperature, protected from light. Slides were then washed quickly with 1× TBS, followed by three additional 10 min 1× TBS washes. Tissue was left to dry at room temperature for ≈1–2 h. To dehydrate tissue sections, slides were placed in a series of ethanol baths: 50%, 50%, 70%, 70%, 90%, 90%, 95%, 95%, 100%, and 100%. Slides were left in each bath for ≈1 min, except for the final 100% ethanol bath, during which slides were left to incubate for at least 3 min. Following dehydration, tissue was then defatted in two xylene baths: 1 min in the first bath and at least 5 min in the second bath. Slides were then mounted in DPX and left to dry overnight at room temperature. *Primary antibodies*: 1 : 250 GFAP (Fisher Scientific, 13-030-0). *Secondary antibodies*: 1 : 500 Alexa Fluor 488 (Guinea Pig, Invitrogen, A-21450).

IR-MALDESI MSI analysis

The NextGen IR-MALDESI source[28] was coupled to and Orbitrap Exploris 240 mass spectrometer (Thermo Fisher Scientific, Bremen, Germany). A 2970 nm mid-IR laser (JGMA, Burlington, MA, United States) was used to desorb neutral tissue from the sample into the electrospray plume. The spatial resolution was set to 0.15 × 0.15 mm (150 μm) and full tissue ablation was observed with laser energy set to approximately 2.1 mJ at 10 pulses-per-burst. The electrospray plume was orthogonal to the sample stage and coaxial with the inlet of the mass spectrometer. The electrospray solvent composition was 50 : 50 MeCN : H_2O with 0.2% FA. Data acquisition voltage (3200–3800 V) and electrospray flowrate (0.9–2.0 μL min^{-1}) varied between analysis days approximately a year apart, and sample analysis order was completely randomized. IR-MALDESI MSI analyses were completed in the positive-ion mode across two mass ranges: *m*/*z* 75–500 and *m*/*z* 200–1000. These two mass ranges were selected according to the analytes of interest, neurotransmitters and lipids, respectively. Two mass ranges were selected in order to maintain the sensitivity of the analyses with lower RF ratios of 7 (neurotransmitters) and 5 (lipids). The RF lens % was set to 70% for small molecules. During data acquisition, the Orbitrap Exploris 240 mass spectrometer's scan rate was synchronized with the IR-MALDESI MSI source.[29] Easy-IC was enabled for all data acquisition wherein radical fluoranthene cations ($M^{\bullet+}$ = *m*/*z* 202.0777) are released, while ions, produced by IR-MALDESI, enter the mass spectrometer. All data were collected in native centroid mode with mass resolution set to 240 000 FWHM at *m*/*z* 200. Automatic gain control (AGC) was disabled, and the injection time was set to 15 ms. Sucrose and endogenous water were utilized as the permeative matrices for all tissue analyses to improve lipid detection,[18] lower experiment time, and reduce technical variability between tissue analyses. The control stroke analyses were completed in May of 2024, and all of the hydrogel-treated sample experiments were conducted in June of 2025. All IR-MALDESI MSI analyses were completed within a month or less of sample preparation to ensure that tissue storage did not influence these analyses or outcomes. Fig. 1 outlines the overall experimental workflow including immunofluorescence staining and IR-MALDESI MSI.

Hydrogel standards were prepared for MS1 analysis to co-validate suspected gel components identified only in the hydrogel-treated samples. Hydrogel standards were prepared for HA-MAP and PSA-MAP treatments. Each standard spotted onto a plain glass slide using a metal spatula with a square ROI drawn around the entire hydrogel spot to ensure no background ions were identified. Hydrogel standards were analyzed in the neurotransmitter mass range (*m*/*z* 75–500) and the lipid mass range (*m*/*z* 200–1000) using the same parameters listed above for the standard IR-MALDESI MSI analyses. All overlapping *m*/*z* values are highlighted in Table S2 alongside each tentative annotation as either "yes" indicating that the *m*/*z* was detected across the entire hydrogel sample and "edge" indicating that the *m*/*z* was localized along the edge of the hydrogel standard. Additionally, rose Bengal dye (Sigma; 10 mg mL^{-1} in PBS) underwent laser illumination at 42 mW using the 520 nm laser for 13 minutes and was analyzed across the neurotransmitter and lipid mass ranges where the dye was spotted on the slide using a metal spatula and a square ROI was run around the entire dye spot to determine on- and off-sample detection. No overlaps were observed for Rose Bengal dye in the control stroke replicates.

File conversion and software

All IR-MALDES MSI files were converted from .RAW format to .mzML format using MSConvert.[30,31] The resulting .mzML files were converted to .imzML image files using the imzML converter.[31] All .imzML files and their respective .ibd files were uploaded to METASPACE[32] and tentatively annotated using the Human Metabolome Database (HMDB endogenous)[33,34] and Lipid Maps Structure Database (LMSD)[35] at a 5% false discovery rate (FDR). Tentative annotations are assigned according to likelihood of presence in the brain and the molecular formula according to the isotopic distribution. All tentative annotations across all tissue samples were combined using Excel, and the resulting list of *m*/*z* values was used to export ion images using MSiReader v2.90 (MSI Software Solutions, LLC, Raleigh, NC).[36,37] All ion images were normalized to the total ion current (TIC) to account for technical variability, experiment conditions, and any inconsistency between analyses. The mass measurement accuracy was kept at ±2 ppm. The cumulative list of on-tissue tentative annotations was sorted according to which metabolites and lipids were likely to be found in mouse

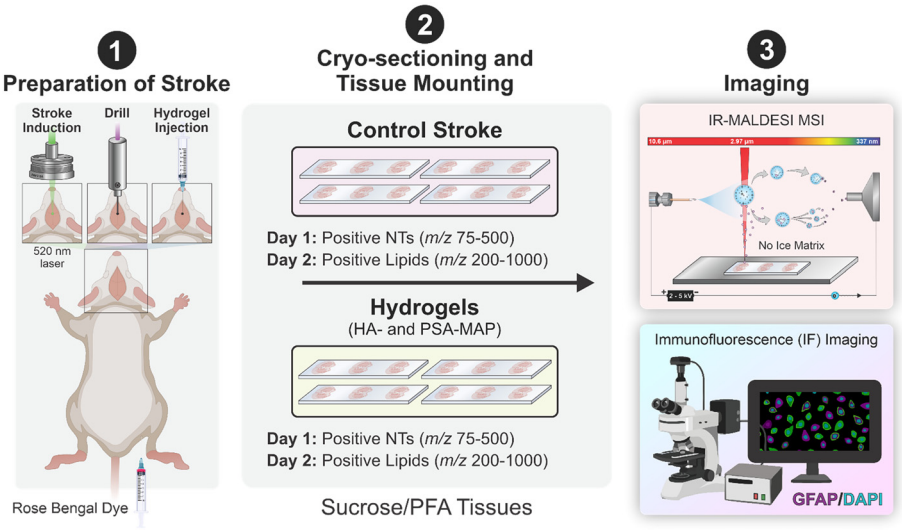

Fig. 1 Experimental overview of PT stroke preparation, tissue sectioning, and IR-MALDESI MSI analysis. Immunofluorescence imaging was completed concurrently using DAPI and GFAP stains in the two hydrogel-treated samples to target nuclei and astrocytes respectively. All tissues were sucrose-embedded and PFA-fixed prior to IR-MALDESI MSI analyses.

brain with some *m*/*z* values counted as probable components of injected synthetic hydrogels.

Statistical testing and analysis

RStudio v485 was used alongside Excel to construct volcano plots and notched box plots, and to perform *t*-tests and other statistical analyses. The Venn diagrams were produced using Venny v2.1.[38] Data for volcano plots were exported using MSiReader v2.90 and formatted with Excel. MSiReader v2.90 was used to extract two similar sized ROIs from each tissue. One ROI was taken from the lesion region of the brain and the other from the same region on the contralateral hemisphere of the brain. The size of the ROI depended on the size of the lesion (infarct and peri-infarct regions). The TIC-normalized, ±2 ppm ion abundance values were extracted from each ROI for all detected *m*/*z* values. For volcano plots, these values were averaged for each biological tissue replicate and the *t*.test function in Excel was used to calculate the *p*-value. Fold change was calculated using the average of the replicate averages wherein the lesion was divided by the contralateral ROI average. All *p*-values were adjusted using the Benjamini–Hochberg correction[39] to reduce the false positives identified in the resulting plots. Statistically significant datapoints had an adjusted *p*-value <0.05 (−log10(adjusted *p*-value) > 1.3) and a fold change less or greater than 1.5 (log2FC </>0.6). *P*-Values were calculated in RStudio using a *t*-test according to the 95% CI and the average of all datapoints.

Results and discussion

In this study, two hyaluronic acid (HA)-based microporous annealed particle (MAP) hydrogel scaffolds were injected into the infarct region of a PT stroke mouse brain model of IS. These HA-MAP-based hydrogels were evaluated according to their impact on lipid and metabolite species within and around the lesion. The two hydrogels evaluated include MAP conjugated with hyaluronic acid (HA-MAP) and MAP conjugated with polysialic acid (PSA-MAP). While both hydrogel materials are immunomodulatory by design, they target different responses in the CNS. The HA-MAP hydrogel modified with norbornene groups delivers the RGD peptide therapeutic to reduce inflammatory monocytes along with an overall reduction of the glial barrier.[21] The PSA-MAP hydrogel modification specifically targets inhibitory Siglec receptors to facilitate immunomodulation for CNS regeneration.[27] These hydrogel-treated mice were evaluated against control stroke mice without any hydrogel scaffold injected into the infarct region-of-interest (ROI). All of these analyses were studied at the late subacute phase of stroke healing (day 15 after stroke induction) in the mouse brain.

IR-MALDESI MSI spatially resolves lipidomic remodeling

To understand how lipids in the brain respond to local ischemia, we utilized a photothrombotic stroke model that produces a local ischemic zone at the site of laser illumination. We selected the contralateral side of each brain section as an internal control to enable comparison among different animals. Our previous work showed that the major lipids categories in normal brain were fatty acyls and glycerophospholipids with 23% and 44% of all lipid detection, respectively, in the positive-ion mode.[18] Herein this study, we find that the overall distribution of detected lipid species was consistent between these two studies. These similarities in lipid coverage is depicted in Fig. 2 with 31% and 53% of lipid detection corresponded to fatty acyls and glycerophospholipids for the control ischemic stroke samples. Fig. 2 details the overall ten-

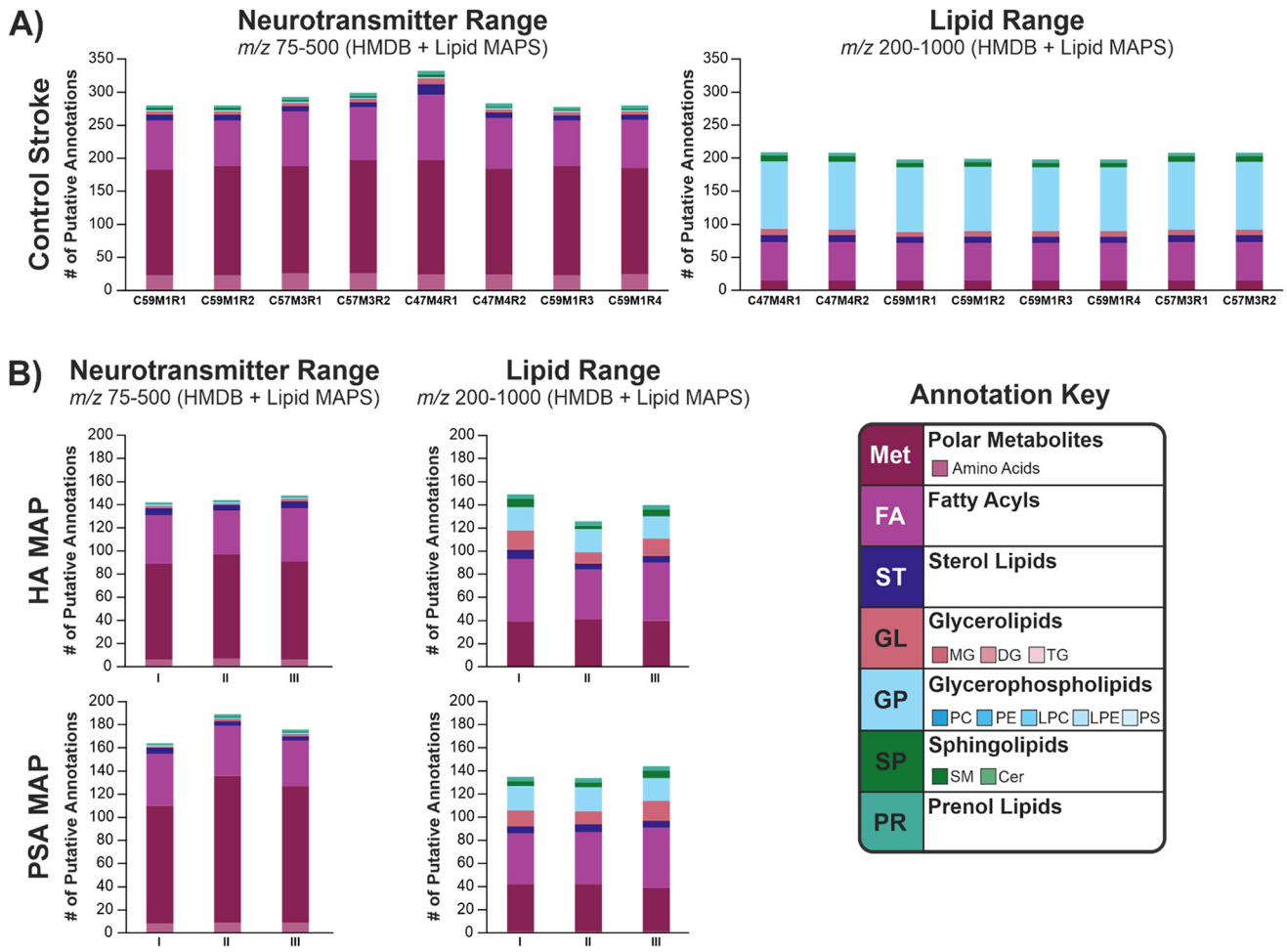

Fig. 2 Detection of lipid and metabolite categories by the (A) control stroke samples (no hydrogel), (B) HA-MAP, and PSA-MAP-treated stroke tissues. All annotations are tentatively identified using METASPACE at 5% false discovery rate (FDR) using the Lipid MAPS Structure Database and HMDB endogenous v4 databases. Tentative annotations are assigned according to MS1 data based on the spatial distribution of signal, theoretical and experimental isotopic distribution, and spatial distribution across the isotopic peaks. All replicates, tentative annotations, and *m/z* values are listed in Table S2.

tative detection of lipid species and polar metabolites across the three tissue preparations (control stroke, HA-MAP, and PSA-MAP). The six lipid categories are defined according to the LMSD:[35] fatty acyls [FA], sterol lipids [ST], glycerolipids [GL], glycerophospholipids [GP], sphingolipids [SP], and prenol lipids [PR]. The *y*-axis accounts for the total tentative annotations found in each preparation across all biological replicates. The number of tentative annotations in each respective category is listed above each bar in the chart.

Lipid detection was consistent between the control stroke replicates and between the hydrogel-treated replicates. The decrease in tentative annotations between the control stroke and hydrogel-treated stroke samples is attributed to the time between analyses. No observable differences were found between the two hydrogel treatments with respect to lipid and metabolite category detection. Reflection plots were compiled using MSiReader using the averaged scans from the ipsilateral and contralateral ROIs in Fig. S1 across the neurotransmitter and lipid mass ranges. To gain further understanding of underlying biological responses to IS with the use of HA-MAP and PSA-MAP hydrogels, IF staining was completed using DAPI and GFAP to the nuclei and astrocytes, respectively. These stains were selected in order to visualize cellular infiltration into the infarct and astroglial response. In this study, understanding the initial cellular response is essential to evaluate how well these hydrogels improve wound healing. IR-MALDESI MSI allows for these findings to be improved upon as MSI provides deeper understanding as to which lipids and metabolites are responding to the inflammation and damage in the lesion. Fig. 3A shows a colocalization plot of three key lipids and metabolites. These images are split into three different colors (red, blue, and green) which correspond to a given lipid or metabolite localized within a specific region or region across the tissue. Glycerol tripropanoate is highlighted blue to show the infarct region of the brain (center of the lesion, damaged tissue from stroke) and may be produced through the formation of the localized ischemia. The red ion images correspond to the peri-infarct region of the lesion

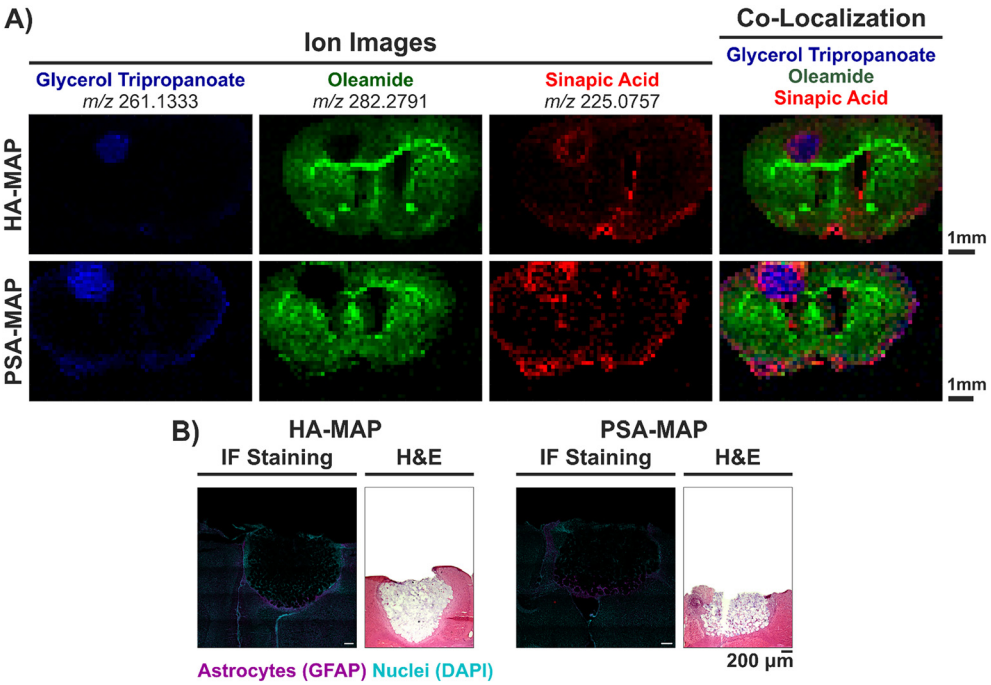

Fig. 3 (A) Representative ion images extracted from MSiReader using the colocalization tool to highlight the infarct region (blue, glycerol tripropanoate), the healthy tissue (green, oleamide), and the peri-infarct region (red, sinapic acid) surrounding the stroke. Key ions were selected according to their presence and localization within these unique regions. (B) The two hydrogel-treated tissues as shown by their immunofluorescence (IF) images and hematoxylin and eosin (H&E) stained images. IF images were produced using glial fibrillary acidic protein (GFAP; astrocytes, purple) and 4′,6-diamidino-2-phenylindole (DAPI; nuclei, green). Off tissue regions of the H&E staining were erased to highlight the on-tissue ROI. Additional IF stained images are available in Fig. S2 of the SI attached.

where healing is occurring, and astrocyte levels are higher. This lipid, sinapic acid, has been known to possess wound healing properties in diabetes.[40] In these diabetes studies, gels loaded with sinapic acid were used to heal skin lesions on rats.[40] These gels improved healing through increased collagen content and decreased malondialdehyde (MDA).[40] Oleamide covers the rest of the tissue, without localized ischemia. Increased ion abundance of oleamide is observed across the rest of the tissue including the anterior commissure (aco) and corpus callosum (cc) with decreased abundance directly in the infarct and peri-infarct regions. The full colocalization plot overlays these three species to demonstrate the ability of IR-MALDESI MSI to distinguish regions of the tissue (*e.g.*, healthy, infarct, and peri-infarct) and spatially resolve lipidomic remodeling as a response to ischemic injury. The physical structure of the lesion and surrounding area is shown in Fig. 3B where the IF and H&E-stained images demonstrate the nuclei and astrocyte response to the lesion and physical impact of the hydrogels. The increased ion abundance around the edge of the tissue shown in Fig. 3A (glycerol tripropanoate and sinapic acid) likely results from tissue drying around the exposed edges of the tissue. These increases in ion abundance are more readily observed with ions that have lower ion abundances.

Fig. S2 provides magnified IF stained images of the infarct and peri-infarct ROIs for each hydrogel treatment of the photothrombotic IS lesion. Additional ROIs shown in Fig. S2 highlights the infarct and peri-infarct regions of the lesion.

CNS ischemic injury drives fatty acid accumulation and glycerophospholipid loss

Volcano plots were constructed in Fig. 4A to identify the key lipids or metabolites that had increased or decreased ion abundance within the ipsilateral (lesion) region of the brain relative to the contralateral. The lesion was defined as the infarct and per-infarct region of the brain combined. Each tissue had varying ROI sizes based on the size of the lesion with a similar size and placed ROI on the contralateral side of the brain. This was done to ensure that the same area of the brain was sampled within the same biological replicate (combination of CTX, CPu, and cc). All anatomical regions of the brain were denoted according to the Allen Brain Atlas (coronal).[41] Data setup and calculations were performed in excel as described in the "Methods: statistical testing and analysis". RStudio was used to plot the data and the Benjamini Hochberg correction for *p*-values was completed in excel prior to data upload to reduce false positive results. The top right of each plot is highlighted blue in the background and indicates metabolites and lipids have statistically significantly increased ion abundance within the ipsilateral ROI relative to the contralateral ROI across all biological replicates. Conversely, the top left of each plot is highlighted red in the background. This region of each volcano plot indicates analytes which have stat-

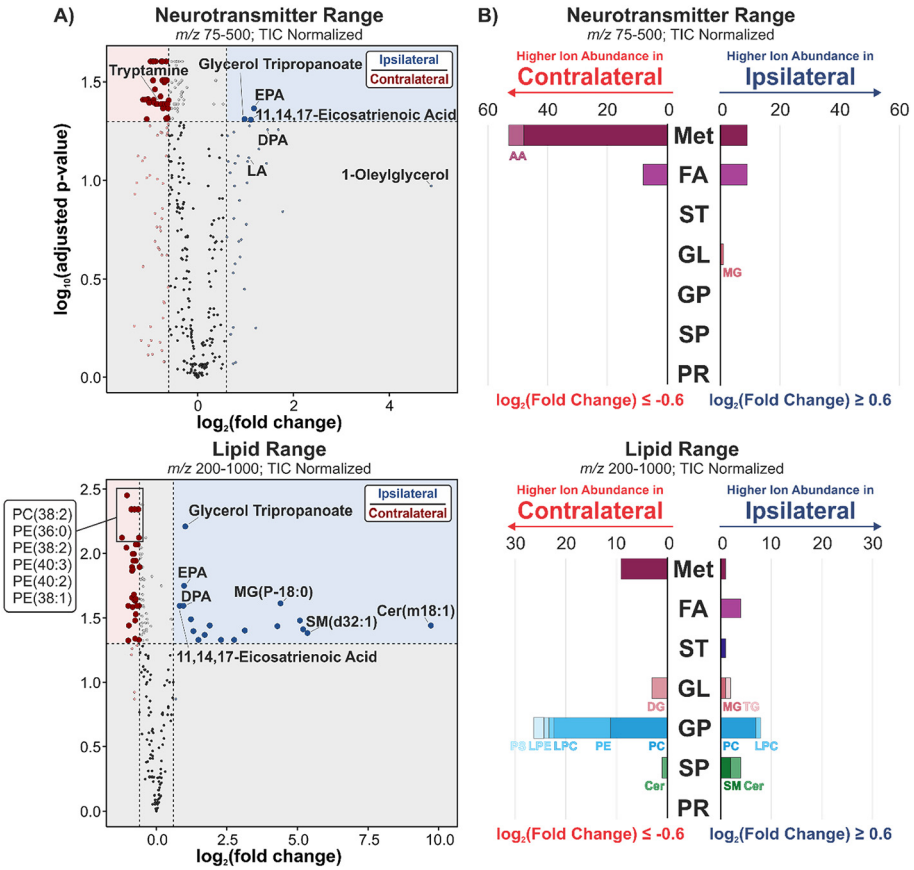

Fig. 4 (A) Volcano plots for two mass ranges *m/z* 75–500 and *m/z* 200–1000 for control stroke (no hydrogel treatment) samples and (B) summary bar charts for lipid categories significantly impacted with respect to fold change. The volcano plots compare the log2(fold change) between the ipsilateral (lesion) region and contralateral (healthy) region of the brain. These regions consist of the infarct and per-infarct region of the brain (lesion) and a similar sized region of interest (ROI) from the contralateral side of the brain. The size of ROIs corresponds to the sample/replicate and varies accordingly to account for only the affected area and the opposite hemisphere of the brain (see Fig. 7). All *p*-values were adjusted according to a Benjamini–Hochberg correction with a cutoff of log10(*p*-value) = 1.3 (*p*-value of 0.05). Key metabolites and lipids of interest are labeled accordingly according to tentative annotations in Table S2. All $-\log_{10}$(Benjamini–Hochberg corrected *p*-values) and $\log_2$(fold changes) are included in Table S2.

istically significantly decreased ion abundances in the lesion relative to contralateral ROI. All grey areas of the plot show metabolites and lipids with no statistically significant increase or decrease in ion abundance in the ipsilateral or contralateral ROI. All analyte responses are listed in Table S2 where any metabolites located solely in the lesion region are noted as "only in lesion" as the fold change could not be determined. Additionally, a majority of these unplotted points are likely components in the hydrogels as they are exclusive to that region. Key lipids and/or metabolites were highlighted and labeled for each plot to demonstrate differences in the responses for each sample. Volcano plot analyses were completed using biological replicates for each control stroke plot (Fig. 4A; $N = 3$ biological; $N = 2$ technical). For each of the control stroke volcano plots (neurotransmitter and lipid ranges), a total of eight samples were analyzed. One of the biological replicates had a total of four technical replicates for the control stroke sample. To ensure no biological replicate dominated the analyses, two of the technical replicates were randomly selected to be excluded. No significant differences were found between these four replicates as is shown in Fig. S3. The superplots in Fig. S4 further investigate the TIC-normalized ion abundances across three biological replicates for metabolites and lipids detected in all conditions with increased ion abundance in the ipsilateral (lesion) region of the brain.

The two volcano plots shown in Fig. 4A, corresponding to the control stroke tissues (no hydrogel treatment) show increased ion abundance of lipid species in the FA category within the ipsilateral region of the brain. Specifically, accumulation of polyunsaturated fatty acids (PUFAs) such as eicosapentaenoic acid (EPA), docosapentaenoic acid (DPA), and linoleic acid (LA) is observed in the lesion as a biological response to inflammation.[42] Previous MSI analyses using matrix-assisted laser desorption/ionization (MALDI) uncovered accumulation of DPA to the ischemic area in a mouse brain model of focal cerebral ischemia.[43] DPA and EPA are both n-3 PUFAs which have anti-inflammatory effects and are implicated in revascularization in stroke.[44] LA has also been reported to accelerate wound repair in topical application to skin lesions by increasing production of free radical nitric

oxide (NO) which increases inflammatory response while activating macrophages and fibrinogen production, and collagen synthesis.[45] In the lipid range of the control stroke model, several PE lipid species had decreased ion abundance in the ipsilateral region relative to the contralateral region whereas SP such as SM(d32:1) and Cer(m18:1) had increased ion abundance in the lesion (ipsilateral region). The SP lipid response to ischemic injury in the brain is consistent with other studies where ceramides may play a critical role in signaling immune cell activation and apoptosis.[46,47] C18-ceramides (*e.g.*, Cer (m18:1)) are known to be one of the most abundant ceramide species in neurons[48] and SM(32:1) was found to be predominately inversely related to IS in one study.[49] The overall accumulation of PUFAs in the infarct and peri-infarct regions may correspond to their role as precursors to lipid mediators.[44] The increased ion abundance of PUFAs in the peri-infarct and infarct regions indicate elevated levels of lipid mediators which play neuroprotective or neurodegenerative roles in post-stroke brain tissue.[44]

Overall lipid category and polar metabolite responses are summarized in Fig. 4B. Six total lipid categories and polar metabolites reflected increased and decreased ion abundances in the PT stroke lesion (ipsilateral region) relative to contralateral region of the tissue. Within these categories, subclasses with several instances of significant fold changes were denoted including AA (amino acids; polar metabolites), MG, DG, TG (mono-, di-, tri-acylglycerol; GL), PC, LPC, PE, LPE, PS (phosphatidylcholine, lysophosphatidylcholine, phosphatidylethanolamine, lysophosphatidylethanolamine, and phosphatidylserine respectively; GP lipid category), SM, and Cer (sphingomyelin and ceramide; SP). For each plot, the left side corresponds to lipids or metabolites which have increased ion abundance in the contralateral (healthy) region relative to the ipsilateral (lesion) region. The right side of each plot shows the count of metabolites and lipids with increased ion abundance within the ipsilateral (lesion) region relative to the contralateral region of the brain. In Fig. 4B, the two control stroke models demonstrate a decrease in polar metabolites and GPs specifically with an increase in FAs and SPs in the lesion region of the brain. The decreased ion abundance of GPs and increased ion abundance of SPs in the lesion relative to contralateral tissue is consistent with literature findings as previously described.[47] Decreased ion abundance in the lesion is consistent with the structural function of GPs and membrane damage associated with IS in the infarct and peri-infarct regions. The findings of Fig. 4B are further summarized in Table 1 where the ten metabolites or lipids with the highest and lowest fold changes are listed. Further details are provided in Table S2 including additional possible molecule annotations and molecular formula.

Immunomodulatory hydrogel scaffolds attenuate inflammatory lipid signatures

The volcano plots in Fig. 5 correspond with the two hydrogel-treated lesions (HA-MAP, and PSA-MAP) across the neurotransmitter (*m*/*z* 75–500) and lipid (*m*/*z* 200–1000) mass ranges. These comparisons result from data collected across three biological replicates. One technical replicate was collected in each of the two mass ranges from the same three biological replicates. In these hydrogel comparisons, the decreased ion abundance in the ipsilateral (lesion) relative to the contralateral region of the brain of lipids and metabolites

Table 1 Summary of the top ten lipids and metabolites with increased or decreased $\log_2$(fold change) values for the control stroke tissues shown in Fig. 4

Neurotransmitter mass range (*m*/*z* 75–500)			Lipid mass range (*m*/*z* 200–1000)		
log2(fold change) (lesion/healthy)	"−log10 (BH-adjusted *P*-value)"	Selected annotation	log2(fold change) (lesion/healthy)	"−log10 (BH-adjusted *P*-value)"	Selected annotation
4.87555766	0.970752098	1-Oleylglycerol	9.72020571	1.441710162	Cer(m18:1)
1.77206836	0.839130309	L-Alpha-aspartyl-L-hydroxyproline	5.355739357	1.383596112	SM(d32:1)
1.685477717	1.259505231	*N*-Hydroxy arachidonoyl amine	5.200895745	1.413143651	PC(O-38:4)
1.467346834	1.259505231	Docosapentaenoic acid	5.09507645	1.477295796	PC(O-36:4)
1.436136057	1.087406645	Sinapic acid	4.390533475	1.609141979	MG(P-18/0)
1.282535945	1.159031266	Kinetin	4.282552463	1.43348826	PC(O-38:5)
1.216801545	0.249517073	7-Ketocholesterol	3.135877074	1.399887704	PC(O-38:6)
1.174469403	1.367288849	Eicosapentaenoic acid	2.76055652	1.327100369	PC(18:0)
1.109237944	1.309037983	11,14,17-Eicosatrienoic acid	2.280845026	1.327100369	15:0 cholesteryl ester
1.085981692	1.276818797	2-Hydroxyadenine	1.895903519	1.441710162	PC(18:1/4:0)
−1.086467802	1.410598036	*N*-Butyl arachidonoyl amine	−0.861599385	1.863628245	LysoPC(P-18:1)
−1.104683451	1.11409344	Melatonin	−0.861927045	1.655793221	PE(28:2)
−1.143803594	0.563713059	2-Methylbutyroylcarnitine	−0.868386861	1.892754047	(*Z*)-5-dodecenyl (*Z*)-5-dodecenoate
−1.144681308	1.410598036	Phenylalanyl-valine	−0.8769738	1.214791609	PC(O-16:1)
−1.153616869	1.099180654	Prolylhydroxyproline	−0.88760345	2.342913041	PE(40:2)
−1.177586718	0.18646659	L-Palmitoylcarnitine	−0.983133356	1.441710162	PC(38:1)
−1.250620987	1.125331811	Phenylalanyl-isoleucine	−1.001365847	1.592697715	PE(28:1)
−1.266812436	0.98652622	Alpha-linolenyl carnitine	−1.007119095	1.32097647	DG(39:0)
−1.306751977	0.929793035	13′-Carboxy-alpha-tocopherol	−1.031718916	2.450161741	PC(38:2)
−1.331575759	0.25854593	*N*-Oleoyl threonine	−1.065519887	2.044845552	PE(30:2)

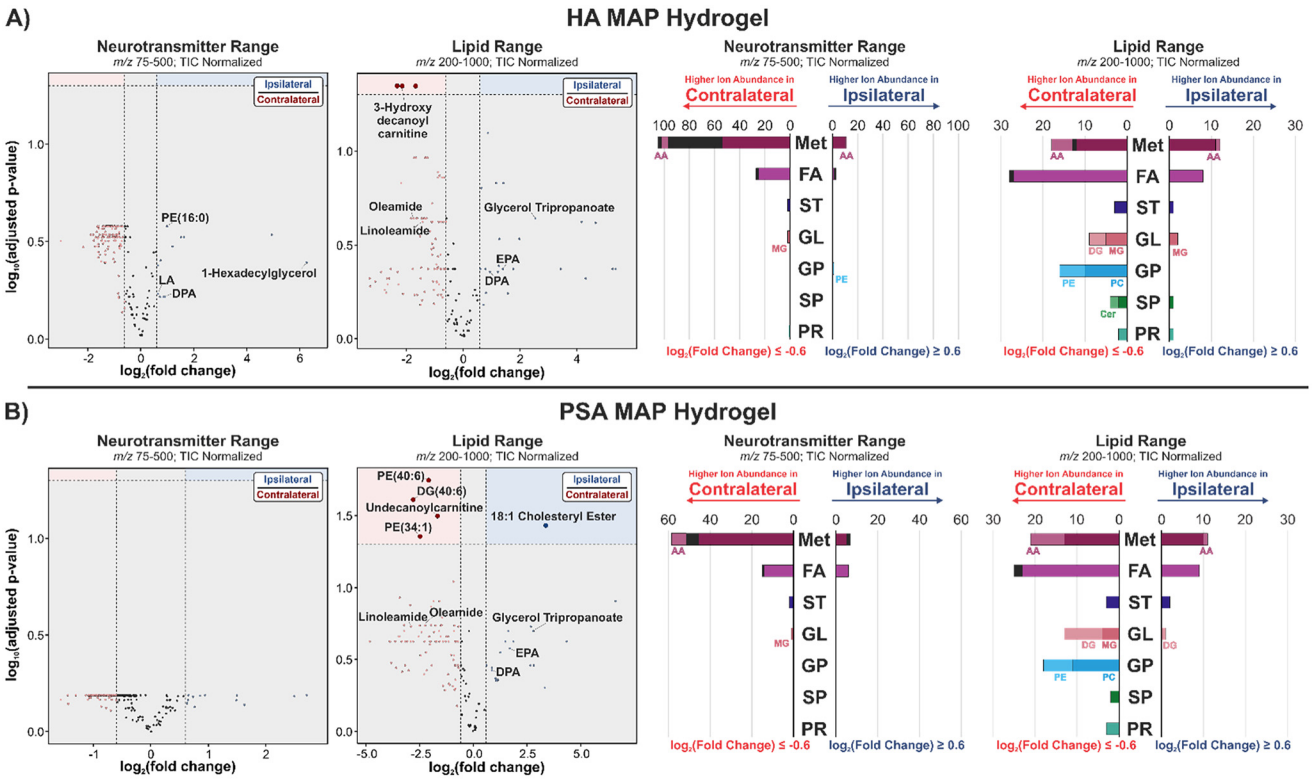

Fig. 5 Volcano plots and summary bar charts for two mass ranges *m/z* 75–500 and *m/z* 200–1000 for both hydrogel-treated samples: (A) HA MAP hydrogel and (B) PSA MAP hydrogel. The volcano plots compare the log2(fold change) between the ipsilateral (lesion) region and contralateral (healthy) region of the brain. These regions consist of the infarct and per-infarct region of the brain (lesion) and a similar sized region of interest (ROI) from the contralateral side of the brain. The size of ROIs corresponds to the sample/replicate and varies accordingly to account for only the affected area and the opposite hemisphere of the brain. All *p*-values were adjusted according to a Benjamini–Hochberg correction with a cutoff of $-\log_{10}(p\text{-value}) = 1.3$ (*p*-value of 0.05). Key metabolites and lipids of interest are labeled accordingly according to tentative annotations in Table S2. The summary bar charts account for all polar metabolites and lipid categories impacted with respect to the $\log_2$fold change. All $-\log_{10}$(Benjamini–Hochberg corrected *p*-values) and $\log_2$(fold changes) are included in Table S2. Additional comparisons between the ipsi- and contralateral regions of the brain between HA-MAP and PSA-MAP are found in Fig. S5 and resulted in no statistically significant differences.

is in part attributed to the matrix effects and attenuated signal-to-noise within the lesion where the hydrogels were injected. The increased ion abundances in the ipsilateral region with no overlapping species in the hydrogel standards were considered more significant in these analyses.

In these plots, a decreased number of statistically significantly impacted metabolites were observed. While the possible impact of hydrogel matrix effects may play a significant role in these findings, this may also indicate that less consistent damage was observed in these treated samples, and lower inflammation or inflammatory response is associated with these samples. These findings correspond to the abilities of the hydrogels to improve wound healing and may aid in healing beyond the inflammatory stage. In particular, the PSA-MAP-treated lesions in the neurotransmitter mass range had the lowest levels of lipid and metabolite response as it pertains to the consistency of these results (*p*-value) and the overall fold change difference between the ipsilateral and contralateral regions. Although several PUFAs had increased ion abundance in the ipsilateral region with respect to fold change, the replicates lacked consistency leading to statistically insignificant findings.

Fig. 5 further summarizes the overall findings with respect to the fold change response of various lipid categories and classes defined by Lipid MAPS Structure Database through bar charts (key found in Fig. 2). Future analyses will need to account for the attenuated lipid responses observed in these hydrogel-treated models of ischemic injury. At present, these findings are consistent between the two mass ranges across both treatments with no significant differences in lipid category increases and decreases in ion abundance.

The lipid and metabolite responses to localized ischemia are further summarized in Tables 2 and 3 where the ten species with the highest and lowest fold changes are listed with their corresponding tentative annotations, $\log_2$(fold change), and $-\log_{10}$(BH-adjusted *p*-values). Table 2 specifically corresponds to the impacts of HA-MAP hydrogel treatment on lipid and metabolite categories, and Table 3 highlights the impacts of the PSA-MAP hydrogel treatment.

In the HA-MAP-treated IS samples, the increased number of metabolites and lipids with significantly increased ion abundances in the lesion (ipsilateral) may be further exacerbated by central nervous system (CNS) foreign body responses (FBR)

Table 2 Summary of the top ten lipids and metabolites with increased or decreased $\log_2$(fold change) values for HA-MAP treated tissues shown in Fig. 5

Neurotransmitter mass range (m/z 75–500)			Lipid mass range (m/z 200–1000)		
log2(fold change) (lesion/healthy)	"−log10 (BH-adjusted *P*-value)"	Selected annotation	log2(fold change) (lesion/healthy)	"−log10 (BH-adjusted *P*-value)"	Selected annotation
6.247928608	0.394337106	1-Hexadecylglycerol	5.352303948	0.371932323	3-Galactosyllactose
1.633098096	0.520875196	(*S*)-Propane-1,2-diol	5.255309712	0.371932323	1-Hexadecylglycerol
1.52107889	0.520875196	Glycerol	4.664038354	0.615958683	PI-Cer(d34:0(2OH))
1.194008055	0.474703166	3-Furoic acid	4.308188659	0.323181021	1-Octadecylglycerol
0.998011693	0.576610565	PE(16:0)	4.167596374	0.621878785	Linolenyl palmitate
0.996930497	0.576610565	Glycerol tripropanoate	3.431033028	0.371932323	D-Maltose/trehalose
0.908190641	0.215945776	Eicosapentaenoic acid	2.540460186	0.641557586	Glycerol tripropanoate
0.850425673	0.215945776	*N*-Acetyldopamine	1.977216362	0.531369305	D-Galactose 6-sulfate
0.743625372	0.403682457	Kinetin	1.763550632	0.371932323	Docosapentaenoic acid
0.729937346	0.215945776	Propionic acid	1.570734293	0.243729675	*N*-Hydroxy arachidonoyl amine
−1.616378905	0.516839498	1*H*-Indole-3-methanamine	−2.529282746	0.371932323	PC(36:1)
−1.64273508	0.576610565	L-Kynurenine	−2.591680374	0.323181021	PC(32:0)
−1.661070435	0.548423211	Oleamide	−2.636513709	0.290536592	PC(38:4)
−1.70542182	0.520875196	Calcitetrol	−2.658852047	0.323181021	5alpha-cholestanone
−1.721214201	0.474703166	*S*-Nitrosoglutathione	−2.685321732	0.245311286	PC(38:6)
−1.781754197	0.505169555	Tryptamine	−2.737820903	0.262561475	PE(32:0)
−1.78705404	0.533385402	*N*-Hydroxy-4-aminobiphenyl	−2.870122522	0.357429423	DG(43:6)
−1.88039825	0.533385402	2-Arachidonylglycerol	−3.071868157	0.305272779	PC(40:6)
−2.178350936	0.473643993	*N*-Oleoyl methionine	−3.254181809	0.279877876	PC(34:0)
−3.016351422	0.50198654	10-Hydroperoxy-*H*4-neuroprostane	−3.271766774	0.323181021	PC(36:2)

Table 3 Summary of the top ten lipids and metabolites with increased or decreased $\log_2$(fold change) values for PSA-MAP treated tissues shown in Fig. 5

Neurotransmitter mass range (m/z 75–500)			Lipid mass range (m/z 200–1000)		
log2(fold change) (lesion/healthy)	"−log10 (BH-adjusted *P*-value)"	Selected annotation	log2(fold change) (lesion/healthy)	"−log10 (BH-adjusted *P*-value)"	Selected annotation
2.711087598	0.187353525	*N*-(*p*-Hydroxyphenethyl)actinidine	1.711058714	0.575229138	Docosapentaenoic acid
2.493525798	0.180189759	3,4-Dihydroxymandelic acid	1.873513088	0.624732404	L-L-Homoglutathione
1.62874817	0.137428249	Lahorenoic acid A	2.661529157	0.459654415	Isoleucyl-serine
1.496484949	0.187353525	3-Furoic acid	2.684395759	0.730553502	Glycerol tripropanoate
1.490827786	0.161488902	Docosapentaenoic acid	2.789607932	0.697589308	*N*-Hydroxy arachidonoyl amine
0.94063598	0.187353525	(*S*)-Propane-1,2-diol	2.82490239	0.460002329	Austdiol
0.858290773	0.184195221	Linoleic acid	3.328936524	0.301946578	D-Maltose/trehalose
0.758338032	0.127453946	Eicosapentaenoic acid	3.374868201	1.429192147	18:1 cholesteryl ester
0.730479084	0.17791931	Linoleoyl ethanolamide	4.345443515	0.624732404	Linolenyl palmitate
0.65449244	0.187353525	Glycerol tripropanoate	6.618807543	0.905440683	CE(22:6)
−1.06887314	0.174229613	Anandamide (20:5,n-3)	−0.129141471	0.041772931	Stearic acid
−1.071538127	0.187353525	1,2,3,4-Tetrahydro-2-methyl-b-carboline	−4.825011526	0.624732404	PC(34:0)
−1.085494539	0.187353525	Tryptamine	−3.886513154	0.624732404	PC(36:1)
−1.089871279	0.187353525	Putrescine	−3.88262639	0.624732404	PC(36:2)
−1.098543434	0.164255952	MG(24:1)	−3.829882045	0.477475135	DG(43:6)
−1.135034478	0.187353525	1-Methylhistamine	−3.649740592	0.624732404	PC(40:6)
−1.309427884	0.187353525	Calcitetrol	−3.58139925	0.442767309	DG(37:1)
−1.435843418	0.142207928	Homocysteine thiolactone	−3.466431669	0.660025936	PC(32:0)
−1.445064217	0.187353525	*N*-Acetylputrescine	−3.437135988	0.660025936	PC(38:6)
−1.568015576	0.164255952	TrHA	−3.424567878	0.929802058	PE(32:0)

and resulting inflammation around the infarct region of the lesion.[50] Schreib *et al*. discusses the impact of FBR through preferentially deposited fatty acids on the surface of unmodified PDMS biomedical implants.[50] This was found to result from molecular and cellular recognition of the foreign surface. The findings by Schreib *et al*. further evaluate that the lipid patterns were consistent in the brain for mice and humans.[50] This investigation of lipid deposition is assessed in Fig. 6 below where six fatty acids detected in this study are visualized through MSI.

The MSI profiles and lipid localization identifies that the control stroke (top two rows; 1–6) has increased ion abundance

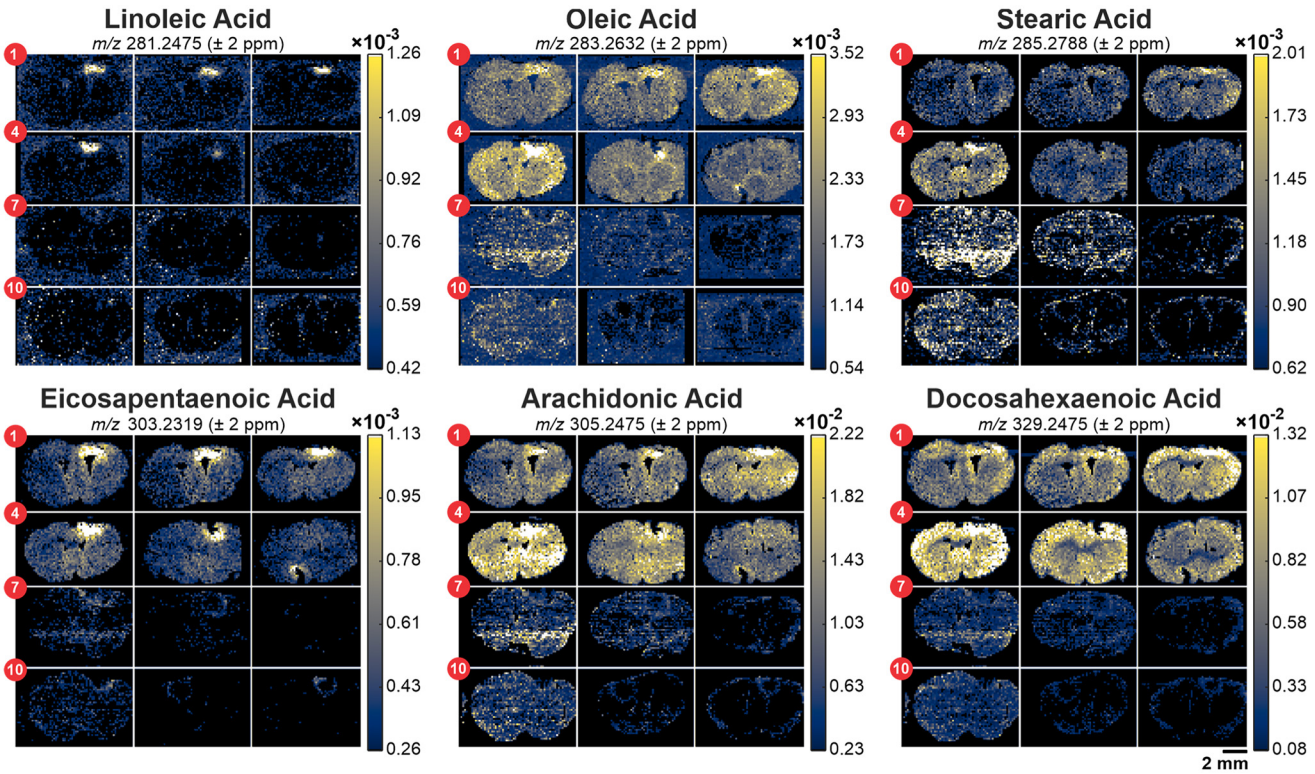

Fig. 6 Extracted TIC-normalized ion images for six key fatty acids across three IS conditions: control stroke (rows 1–2; tissues 1–6), HA-MAP (row 3; tissues 7–9), and PSA-MAP (row 4; tissues 10–12). All images have ±2 ppm mass measurement accuracy and are numbered left to right and top down. All ion images are on the same TIC-normalized ion abundance scale which may impact observable differences for images with lower ion abundances.

in the ipsilateral (lesion) region throughout the infarct and peri-infarct regions. The HA-MAP samples (row 3; 7–9) and PSA-MAP samples (row 4; 10–12) have localization of these lipid species within the peri-infarct region of the tissue surrounding the direct infarction. These findings indicate that fatty acids may be deposited on the surface of the hydrogel injection site as an FBR. The detection of these lipids in the control stroke throughout the infarct region also highlights the previously mentioned matrix effects at the center of the hydrogel injection site where signal is attenuated due to interference from MAPs.

PSA-MAP increases cholesterol esterification consistent with inflammation resolution

In the lipid mass range of Fig. 5, PSA-MAP highlights higher fold changes in addition to the significantly increased ion abundance of the tentative annotation, cholesteryl ester 18:1. The ratio of cholesteryl ester to cholesterol has shown decrease in patients with cardiovascular disorders including IS using blood plasma samples.[51] Across all three replicates of HA-MAP and PSA-MAP, the TIC-normalized ion abundances for this specific cholesteryl ester (18:1) and cholesterol were extracted from the lesion (ipsilateral) and contralateral regions and ratios were calculated using the averages in each ROI. This relationship between these tentative annotations is investigated in Fig. 7 where PSA-MAP shows an increase in the ratio of cholesteryl ester to cholesterol relative to HA-MAP samples in both the lesion (ipsilateral) and contralateral ROIs.

The increased TIC-normalized ion abundance ratio of cholesteryl ester 18:1 and cholesterol, specifically within the lesion (ipsilateral) region supports the our hypothesis that PSA-MAP reduces inflammation *via* efficient conversion of cholesterol to cholesteryl ester.[51,52] This conversion of cholesterol to cholesteryl esters in Huntington's Disease (HD) was investigated in Phillips *et al*. where the authors suggested this mechanism compensates the accumulation of cholesterol in HD.[53] Additionally, Nielsen *et al.* (2016) investigated focal cerebral ischemia in mice using matrix-assisted laser desorption/ionization (MALDI). Accumulation of cholesteryl esters (including cholesteryl ester 18:1) was observed in ischemic sites of the brain during inflammation resolution time points.[43] Further, Ouyang *et al*. developed and analyzed this PSA-MAP hydrogel for treatment of IS and found that it led to decreased inflammation in the peri-infarct region of the ipsilateral (lesion) region of the brain.[27] Additionally, studies have found that in the chronic stage post-stroke, accumulation of free cholesterol leads to formation of cholesterol crystals.[54] These findings are consistent with cholesterol dysregulation and overwhelm of cellular buffering abilities including esterification of free cholesterol.[54] Conversely, cholesteryl esters are also the primary form of cholesterol stored in foam cells.[55] As foam cells accumulate from macrophages and cholesteryl esters,

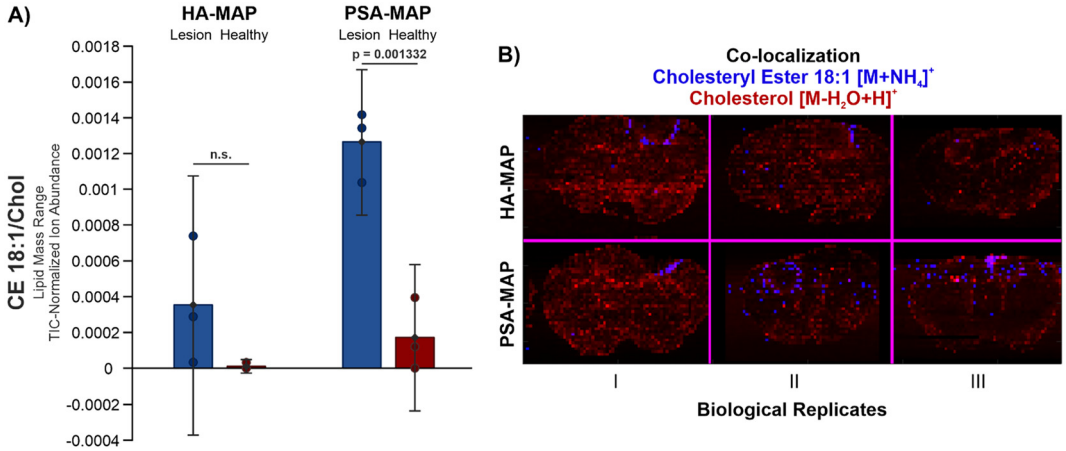

Fig. 7 Hydrogel modulation of cholesterol metabolism and storage is shown through (A) bar charts were constructed to show the ratio of the TIC-normalized ion abundance of tentatively annotated cholesteryl ester 18:1 and cholesterol in the ipsilateral (lesion) and contralateral (healthy) regions of the brain. Each bar chart was constructed using the average TIC-normalized ion abundance in an ipsilateral and contralateral ROI for three biological replicates. The error bars represent the 95% confidence interval and *p*-values were calculated in excel using the "two-sample assuming unequal variances" one-tailed *t*-test in Analysis ToolPak. Limited replicates in this study limit conclusions in this analysis. The colocalization plot in (B) shows the spatial distribution of cholesteryl ester 18:1 and cholesterol across the three biological replicates of HA-MAP and PSA-MAP samples. All values and ion images were TIC-normalized within ±2 ppm mass measurement accuracy.

atherosclerosis may begin to develop or worsen.[55] Further analyses with additional biological replicates and time points will be required to validate these potential findings and investigate the role of cholesterol and its metabolites in this model of IS and wound healing. Immunofluorescence staining will be required to gain deeper insight into macrophage localization.

Conclusions

These analyses implemented IR-MALDESI MSI to spatially resolve lipidomic remodeling as a response to localized ischemia in the brain. This model of CNS ischemic injury resulted in the accumulation of polyunsaturated fatty acids and sphingolipids (*e.g.*, ceramides and sphingomyelin) as a response to resolve inflammation surrounding the infarction. Conversely, localized CNS ischemia is hallmarked by the depletion of membrane lipids including glycerophospholipids (*e.g.*, phosphatidylethanolamines and phosphatidylcholines) as a response to membrane damage.

Biomaterials such as microporous annealed particles (HA-MAP and PSA-MAP) demonstrated their potential to reduce inflammatory lipid species in the infarction and improve the efficiency of cholesterol esterification to restore balance of cholesterol metabolism in wound healing. However, future analyses will be required to understand the impacts of biomaterials with respect to matrix effects and foreign body responses in these applications.

These results suggest that lipid remodeling following CNS ischemia reflects both membrane degradation as well as immune activation. Immunomodulatory biomaterials may further shift their metabolic landscape towards inflammation resolution and repair.

Author contributions

M. F. W. wrote the original manuscript, designed IR-MALDESI MSI experiments, acquired, analyzed, and interpreted MSI data. Y. O. revised the original manuscript, performed all animal experiments including photothrombotic stroke, hydrogel injection, tissue removal, and sucrose/PFA preparation, performed IF staining procedures and imaging. T. S. conceived the methodology, designed all animal experiments, designed all biomedical engineering approaches including the hydrogels tested in this study, and revised the manuscript. D. C. M. conceived the methodology, designed experiments, data analysis, and revised the manuscript.

Conflicts of interest

D. C. M. is part owner of MSI Software Solutions, LLC, which produces MSiReader (https://www.msireader.com) – software that was used in part for this study.

Data availability

All .imzML files from IR-MALDESI analyses may be found on METASAPCE at: https://metaspace2020.org/project/Ischemic_Stroke_2026.

Supplementary information (SI): the excel file attached includes all tentative MS1 annotations for each tissue in addition to hydrogel standards overlaps, and calculated log2 (fold change) and Benjamini–Hochberg corrected *p*-values. Excel document – Table S2. See DOI: https://doi.org/10.1039/d6an00089d.

Acknowledgements

The authors gratefully acknowledge the financial support provided by the National Institutes of Health (R01GM087964) and North Carolina State University. All IR-MALDESI MSI experiments were performed in the Molecular Education, Technology, and Research Innovation Center (METRIC). All IF measurements and animal experiments were performed at Duke University.

References

1 Q. Wang, *et al.*, Impaired membrane lipids in ischemic stroke: a key player in inflammation and thrombosis, *J. Neuroinflammation*, 2025, **22**, 144.
2 C. Iadecola, M. S. Buckwalter and J. Anrather, Immune responses to stroke: mechanisms, modulation, and therapeutic potential, *J. Clin. Invest.*, 2020, **130**, 2777–2788.
3 Y. Wang, *et al.*, Metabolic reprogramming in ischemic stroke: when glycolytic overdrive meets lipid storm, *Cell Death Dis.*, 2025, **16**, 788.
4 C. Iadecola, M. S. Buckwalter and J. Anrather, Immune responses to stroke: mechanisms, modulation, and therapeutic potential, *J. Clin. Invest.*, 2020, **130**, 2777–2788.
5 M. Osetrova, *et al.*, Lipidome atlas of the adult human brain, *Nat. Commun.*, 2024, **15**, 4455.
6 P. Prakash, C. E. Randolph, K. A. Walker and G. Chopra, Lipids: Emerging Players of Microglial Biology, *Glia*, 2025, **73**, 657–677.
7 M. Osetrova, *et al.*, Lipidome atlas of the adult human brain, *Nat. Commun.*, 2024, **15**, 4455.
8 J. Panezai and T. van Dyke, Polyunsaturated Fatty Acids and Their Immunomodulatory Actions in Periodontal Disease, *Nutrients*, 2023, **15**, 821.
9 Y. Sun, *et al.*, Lipid metabolism in microglia: Emerging mechanisms and therapeutic opportunities for neurodegenerative diseases (Review), *Int. J. Mol. Med.*, 2025, **56**, 1–19.
10 W. T. Andrews, *et al.*, In situ metabolite and lipid analysis of GluN2D−/− and wild-type mice after ischemic stroke using MALDI MSI, *Anal. Bioanal. Chem.*, 2020, **412**, 6275–6285.
11 I. A. Mulder, *et al.*, Distinguishing core from penumbra by lipid profiles using Mass Spectrometry Imaging in a transgenic mouse model of ischemic stroke, *Sci. Rep.*, 2019, **9**, 1090.
12 K. O. Schubert, F. Weiland, B. T. Baune and P. Hoffmann, The use of MALDI-MSI in the investigation of psychiatric and neurodegenerative disorders: A review, *Proteomics*, 2016, **16**(11–12), 1747–1758.
13 E. Fridjonsdottir, *et al.*, Mass spectrometry imaging identifies abnormally elevated brain L-DOPA levels and extrastriatal monoaminergic dysregulation in L-DOPA–induced dyskinesia, *Sci. Adv.*, 2021, **7**, eabe5948.
14 L. I. L. Maciel, *et al.*, A new approach for the analysis of amino acid neurotransmitters in mouse brain tissues using DESI imaging, *Int. J. Mass Spectrom.*, 2022, **471**, 116730.
15 Y. Sugiura, E. Sugiyama and M. Suematsu, DESI-based imaging mass spectrometry in forensic science and clinical diagnosis, in *Ambient Ionization Mass Spectrometry in Life Sciences*, Elsevier, 2020, pp. 107–118. DOI: 10.1016/B978-0-12-817220-9.00004-7.
16 H. Bai, K. E. Linder and D. C. Muddiman, Three-dimensional (3D) imaging of lipids in skin tissues with infrared matrix-assisted laser desorption electrospray ionization (MALDESI) mass spectrometry, *Anal. Bioanal. Chem.*, 2021, **413**, 2793–2801.
17 H. Bai, A. S. Arnedo, Y. Liu, T. Segura and D. C. Muddiman, Unraveling the molecular dynamics of wound healing: integrating spatially resolved lipidomics and temporally resolved proteomics, *Anal. Bioanal. Chem.*, 2025, **417**, 3299–3314.
18 M. F. Wang, *et al.*, Lipidomic Analysis of Mouse Brain to Evaluate the Efficacy and Preservation of Different Tissue Preparatory Techniques by IR-MALDESI-MSI, *J. Am. Soc. Mass Spectrom.*, 2023, **34**, 869–877.
19 M. F. Wang, Y. Ouyang, T. Segura and D. C. Muddiman, Optimizing neurotransmitter pathway detection by IR-MALDESI-MSI in mouse brain, *Anal. Bioanal. Chem.*, 2024, **416**(18), 4207–4218.
20 K. Erning and T. Segura, Materials to promote recovery after stroke, *Curr. Opin. Biomed. Eng.*, 2020, **14**, 9–17.
21 N. V. Phan, E. M. Rathbun, Y. Ouyang, S. T. Carmichael and T. Segura, Biology-driven material design for ischaemic stroke repair, *Nat. Rev. Bioeng.*, 2023, **2**, 44–63.
22 T. Segura, *et al.*, Crosslinked hyaluronic acid hydrogels: a strategy to functionalize and pattern, *Biomaterials*, 2005, **26**, 359–371.
23 K. Erning, *et al.*, Delivery of Angiogenic Therapy from Flowable Hyaluronic Acid Porous Scaffolds Results in Functional Improvement without Anti–Inflammatory Agents, *Adv. Funct. Mater.*, 2025, **35**, 2500696.
24 K. Erning, *et al.*, Delivery of Angiogenic Therapy from Flowable Hyaluronic Acid Porous Scaffolds Results in Functional Improvement without Anti–Inflammatory Agents, *Adv. Funct. Mater.*, 2025, **35**, 2500696.
25 A. N. Clarkson, B. S. Huang, S. E. MacIsaac, I. Mody and S. T. Carmichael, Reducing excessive GABA-mediated tonic inhibition promotes functional recovery after stroke, *Nature*, 2010, **468**, 305–309.
26 A. R. Anderson, E. Nicklow and T. Segura, Particle fraction is a bioactive cue in granular scaffolds, *Acta Biomater.*, 2022, **150**, 111–127.
27 Y. Ouyang, S. Che, H. Newman, K. Poysungnoen and T. Segura, Polysialic Acid Presentation on Microporous Scaffolds Supports Neural Repair after Ischemic Stroke, *bioRxiv*, 2025, preprint, 1–35, DOI: 10.1101/2025.09.30.674064.
28 K. T. Knizner, *et al.*, Next-Generation Infrared Matrix-Assisted Laser Desorption Electrospray Ionization Source for Mass Spectrometry Imaging and High-Throughput Screening, *J. Am. Soc. Mass Spectrom.*, 2022, **33**(11), 2070–2077.
29 K. T. Knizner, *et al.*, Optimized C-Trap Timing of an Orbitrap 240 Mass Spectrometer for High-Throughput

Screening and Native MS by IR-MALDESI, *J. Am. Soc. Mass Spectrom.*, 2022, **33**, 328–334.
30 A. M. Race, I. B. Styles and J. Bunch, Inclusive sharing of mass spectrometry imaging data requires a converter for all, *J. Proteomics*, 2012, **75**, 5111–5112.
31 M. C. Chambers, *et al.*, A cross-platform toolkit for mass spectrometry and proteomics, *Nat. Biotechnol.*, 2012, **30**, 918–920.
32 A. Palmer, *et al.*, FDR-controlled metabolite annotation for high-resolution imaging mass spectrometry, *Nat. Methods*, 2017, **14**, 57–60.
33 D. S. Wishart, *et al.*, HMDB 4.0: the human metabolome database for 2018, *Nucleic Acids Res.*, 2018, **46**, D608–D617.
34 D. S. Wishart, *et al.*, HMDB: the Human Metabolome Database, *Nucleic Acids Res.*, 2007, **35**, D521–D526.
35 E. Fahy, M. Sud, D. Cotter and S. Subramaniam, LIPID MAPS online tools for lipid research, *Nucleic Acids Res.*, 2007, **35**, W606–W612.
36 M. T. Bokhart, M. Nazari, K. P. Garrard and D. C. Muddiman, MSiReader v1.0: Evolving Open-Source Mass Spectrometry Imaging Software for Targeted and Untargeted Analyses, *J. Am. Soc. Mass Spectrom.*, 2018, **29**, 8–16.
37 G. Robichaud, K. P. Garrard, J. A. Barry and D. C. Muddiman, MSiReader: An Open-Source Interface to View and Analyze High Resolving Power MS Imaging Files on Matlab Platform, *J. Am. Soc. Mass Spectrom.*, 2013, **24**, 718–721.
38 J. C. Oliveros, Venny, An Interactive Tool for Comparing Lists with Venn's Diagrams, References - Scientific Research Publishing, Csic, 2007, https://bioinfogp.cnb.csic.es/tools/venny/index.html.
39 Y. Benjamini, R. Heller and D. Yekutieli, Selective inference in complex research, *Philos. Trans. R. Soc., A*, 2009, **367**, 4255–4271.
40 K. Kaltalioglu, Sinapic acid-loaded gel accelerates diabetic wound healing process by promoting re-epithelialization and attenuating oxidative stress in rats, *Biomed. Pharmacother.*, 2023, **163**, 114788.
41 M. Hawrylycz, *et al.*, *The allen brain atlas*, in *Springer Handbook of Bio-/Neuroinformatics*, 2014. DOI: 10.1007/978-3-642-30574-0_62.
42 S. K. Venø, E. B. Schmidt and C. S. Bork, Polyunsaturated Fatty Acids and Risk of Ischemic Stroke, *Nutrients*, 2019, **11**, 1467.
43 M. M. B. Nielsen, *et al.*, Mass spectrometry imaging of biomarker lipids for phagocytosis and signalling during focal cerebral ischaemia, *Sci. Rep.*, 2016, **6**, 39571.
44 A. Kloska, M. Malinowska, M. Gabig-Cimińska and J. Jakóbkiewicz-Banecka, Lipids and Lipid Mediators Associated with the Risk and Pathology of Ischemic Stroke, *Int. J. Mol. Sci.*, 2020, **21**, 3618.
45 J. R. Silva, *et al.*, Wound Healing and Omega-6 Fatty Acids: From Inflammation to Repair, *Mediators Inflammation*, 2018, **2018**, 1–17.
46 N. Sun, R. F. Keep, Y. Hua and G. Xi, Critical Role of the Sphingolipid Pathway in Stroke: a Review of Current Utility and Potential Therapeutic Targets, *Transl. Stroke Res.*, 2016, **7**, 420–438.
47 Q. Wang, *et al.*, Impaired membrane lipids in ischemic stroke: a key player in inflammation and thrombosis, *J. Neuroinflammation*, 2025, **22**, 144.
48 A. Mohamud Yusuf, *et al.*, Signaling roles of sphingolipids in the ischemic brain and their potential utility as therapeutic targets, *Neurobiol. Dis.*, 2024, **201**, 106682.
49 L. Lind, *et al.*, A Multi-Cohort Metabolomics Analysis Discloses Sphingomyelin (32:1) Levels to be Inversely Related to Incident Ischemic Stroke, *J. Stroke Cerebrovasc. Dis.*, 2020, **29**, 104476.
50 C. C. Schreib, *et al.*, Lipid Deposition Profiles Influence Foreign Body Responses, *Adv. Mater.*, 2023, **35**, e2205709.
51 M. J. Gerl, *et al.*, Cholesterol is Inefficiently Converted to Cholesteryl Esters in the Blood of Cardiovascular Disease Patients, *Sci. Rep.*, 2018, **8**, 14764.
52 P. M. Cazita, D. F. Barbeiro, A. I. S. Moretti, E. C. R. Quintão and F. G. Soriano, Human cholesteryl ester transfer protein expression enhances the mouse survival rate in an experimental systemic inflammation model: A novel role for CETP, *Shock*, 2008, **30**, 590–595.
53 G. R. Phillips, *et al.*, Cholesteryl ester levels are elevated in the caudate and putamen of Huntington's disease patients, *Sci. Rep.*, 2020, **10**, 20314.
54 Q. Zhao, *et al.*, Cholesterol metabolic reprogramming mediates microglia-induced chronic neuroinflammation and hinders neurorestoration following stroke, *Nat. Metab.*, 2025, **7**, 2099–2116.
55 M. F. Linton, *et al.*, The Role of Lipids and Lipoproteins in Atherosclerosis, *Science*, 2019, **111**, 1–101.